Composited analyses of the chemical and physical characteristics of co-polluted days by ozone and $PM_{2.5}$ over 2013-2020 in the Beijing–Tianjin–Hebei region

Huibin Dai[1], Hong Liao[1*], Ke Li[1], Xu Yue[1], Yang Yang[1], Jia Zhu [1], Jianbing Jin[1], Baojie Li[1], Xingwen Jiang[2]

[1]Jiangsu Key Laboratory of Atmospheric Environment Monitoring and Pollution Control, Jiangsu Collaborative Innovation Center of Atmospheric Environment and Equipment Technology, School of Environmental Science and Engineering, Nanjing University of Information Science & Technology, Nanjing 210044, China

[2]Institute of Plateau Meteorology, China Meteorological Administration, Chengdu, Sichuan 610072, China

*Correspondence to: Hong Liao (hongliao@nuist.edu.cn)

Abstract.

The co-polluted days by ozone (O_3) and $PM_{2.5}$ (particulate matter with an aerodynamic equivalent diameter of 2.5 μm or less) (O_3&$PM_{2.5}$PD) were frequently observed in the Beijing–Tianjin–Hebei (BTH) region in warm seasons (April-October) of 2013-2020. We applied the 3-D global chemical transport model (GEOS-Chem) to investigate the chemical and physical characteristics of O_3&$PM_{2.5}$PD by composited analyses of such days that were captured by both the observations and the model. Model results showed that, when O_3&$PM_{2.5}$PD occurred, the concentrations of hydroxyl radical and total oxidant, sulfur oxidation ratio, and nitrogen oxidation ratio were all high, and the concentrations of sulfate at the surface were the highest among all pollution types. We also found unique features in vertical distributions of aerosols during O_3&$PM_{2.5}$PD; concentrations of $PM_{2.5}$ decreased with altitude near the surface but remained stable at 975-819 hPa. Process analyses showed that secondary aerosols (nitrate, ammonium and sulfate) had strong chemical productions at 913-819 hPa, which were then transported downward, resulting in the quite uniform vertical profiles at 975-819 hPa in O_3&$PM_{2.5}$PD. The weather patterns for O_3&$PM_{2.5}$PD were characterized by anomalous high-pressure system at 500 hPa as well as strong southerlies and high RH at 850 hPa. The latter resulted in the strong chemical productions around 850 hPa in O_3&$PM_{2.5}$PD. The physical and chemical characteristics of O_3&$PM_{2.5}$PD are quite different from those of polluted days by either O_3 alone or $PM_{2.5}$ alone, which have important implications for air quality management.

Keywords: Co-occurrence, Ozone and $PM_{2.5}$, Pollution, Meteorological parameters.

1. Introduction

Surface ozone (O_3) and $PM_{2.5}$ (particulate matter with an aerodynamic equivalent diameter of 2.5 micrometers or less) are important air pollutants in the atmosphere that have harmful effects on public health (Gao and Ji, 2018; Jiang et al., 2019), ecosystems (Ren et al., 2011; Yue et al., 2017), and crops (Wang et al., 2005; Wang et al., 2007). Surface O_3 is a secondary pollutant produced by photochemical oxidation of volatile organic compounds (VOCs) and nitrogen oxides ($NO_x \equiv NO+NO_2$) in the presence of intense ultraviolet light, and the major $PM_{2.5}$ components (nitrate (NO_3^-), ammonium (NH_4^+), sulfate (SO_4^{2-}), black carbon (BC), organic carbon (OC)) are mainly caused by anthropogenic emissions of aerosols and aerosol precursors. Although surface O_3 and $PM_{2.5}$ have different formation mechanisms, they are coupled through the common precursors (NO_x and VOCs) and photochemical reactions (Chu et al., 2020). Since 2013, stringent clean air actions have been implemented to improve air quality in China (State Council of the People's Republic of China, 2013, 2018). However, O_3 concentrations increased unexpectedly, while $PM_{2.5}$ concentrations decreased drastically in the past years (Li et al., 2019). The co-polluted days by O_3 and $PM_{2.5}$ (concentrations of both O_3 and $PM_{2.5}$ exceed the national air quality standards on the same day, hereafter referred to as O_3&$PM_{2.5}$PD) were also reported (Dai et al., 2019). Therefore, it is fundamental to examine the chemical and physical characteristics of O_3&$PM_{2.5}$PD.

The Beijing–Tianjin–Hebei (BTH) region is the most populated region in northern China. In the past few years, concentrations of O_3 and $PM_{2.5}$ in the BTH were among the highest in China. The observations from China National Environmental Monitoring Center (CNEMC) showed that the mean and maximum MDA8 (daily maximum 8-h average) O_3 in North China in summer of 2019 were 83 ppb and 129 ppb, respectively, and the summer mean MDA8 O_3 increased with a trend of 3.3 ppb a^{-1} over 2013–2019 (Li et al., 2020). Gong et al. (2020) reported that O_3 polluted days (i.e., MDA8 O_3

concentration exceeds 80 ppb) in May-July in the BTH increased from 35 days in the year of 2014 to 56 days in 2018. As for observed $PM_{2.5}$, the concentration averaged over BTH had a decreasing trend of 10 $\mu g\ m^{-3}\ yr^{-1}$ over 2013-2019, and the mean value was $79 \pm 17\ \mu g\ m^{-3}$ over these years (Li et al., 2020). BTH also had the highest frequency and intensity of severe haze pollution days (i.e., days with daily mean $PM_{2.5}$ concentration exceeding 150 $\mu g\ m^{-3}$) in China from 2013 to 2017, with an observed mean frequency of 21.2 $d\ yr^{-1}$ and an observed mean intensity of 231.6 $\mu g\ m^{-3}$ (Dang and Liao, 2019).

The interactions between O_3 and $PM_{2.5}$ have been reported in previous studies. Zhu et al. (2019) examined the spatial-temporal characteristics of the correlations between observed O_3 and $PM_{2.5}$ at 1497 sites in China for 2016 and found that O_3–$PM_{2.5}$ had the highest positive correlations (correlation coefficients > +0.7) in July in southern China and the largest negative correlations (r values < −0.5) during January in northern China. Li et al. (2019) used the GEOS-Chem model to analyze the O_3-$PM_{2.5}$ relationship in northern China and found that O_3 production was suppressed under high $PM_{2.5}$ conditions ($PM_{2.5}$ concentrations > 60 $\mu g\ m^{-3}$) because of the reactive uptake of hydrogen oxide radicals (HO_x) by aerosol particles. Chu et al. (2020) analyzed the observed daily $PM_{2.5}$ and O_3 concentrations in 114 cities in China during years of 2013-2018 and found that the correlations between O_3 and $PM_{2.5}$ tended to change from negative in 2013 to positive in 2018 in China as air quality improved.

Few previous studies have examined the co-occurrence of O_3 and $PM_{2.5}$ pollution (MDA8 O_3 > 80 ppb and $PM_{2.5}$ > 75 $\mu g\ m^{-3}$). Zong et al. (2021) used the obliquely rotated principal component analysis in the T-mode (T-PCA) method to identify the synoptic weather pattern associated with O_3&$PM_{2.5}$PD in eastern China during summer of 2015–2018, and found that O_3&$PM_{2.5}$PD were associated with a stable

western Pacific subtropical high ridge, which brought warm and moist air flow from the East China Sea to the eastern China to promote hygroscopic growth of fine particulate matter in BTH and northern YRD. Dai et al. (2021) analyzed O_3&$PM_{2.5}$PD in the YRD for April-October of 2013-2019 by using observations and reported that the co-polluted days occurred mainly in April (29.6% of co-polluted days occurred in April), May (23.0%), June (19.5%), and October (10.8%) under meteorological conditions of higher relative humidity, higher surface air temperature, and lower wind speed relative to the days with O_3 pollution alone. Qin et al. (2021) investigated O_3&$PM_{2.5}$PD by using the hourly observed concentrations of water-soluble ions, OC, and elemental carbon (EC) in 2019 in cities of Nanjing and Changzhou. They found that inorganic aerosols mainly existed as NH_4NO_3 and the correlation coefficients between the secondary components NO_3^-, NH_4^+, and SO_4^{2-} were relatively high during O_3&$PM_{2.5}$PD in 2019, indicating a significant formation of secondary inorganic aerosols. Although these studies have discussed the meteorological conditions and some chemical characteristics of O_3&$PM_{2.5}$PD, the understanding of O_3&$PM_{2.5}$PD was quite limited because of the limited observations of chemical species involved.

In this work, we take advantage of the comprehensive chemical mechanism of the global chemical transport model to have better understanding of O_3&$PM_{2.5}$PD. We apply the 3-D global chemical transport model (GEOS-Chem) to simulate O_3&$PM_{2.5}$PD in BTH in years of 2013-2020, and investigate the chemical and physical characteristics of O_3&$PM_{2.5}$PD by composited analyses of such days that are captured by both the observations and the model. The objectives of this study are: 1) to examine the underlying chemical mechanisms for O_3&$PM_{2.5}$PD in BTH for warm seasons (April-October) of 2013-2020 by comparing O_3&$PM_{2.5}$PD with polluted days by O_3 alone or by $PM_{2.5}$ alone, and 2) to identify the weather patterns that are

associated with O_3&$PM_{2.5}$PD in BTH. The observations, the reanalyzed meteorological data, the GEOS-Chem model, and the process analysis are described in Section 2. The observed O_3&$PM_{2.5}$PD are presented in Section 3.1. The evaluation of simulated concentrations of O_3 and $PM_{2.5}$ as well as the simulated pollution days by O_3 and/or $PM_{2.5}$ are shown in Section 3.2. The underlying mechanisms of O_3&$PM_{2.5}$PD are shown in Section 3.3. In Section 3.4, the meteorological conditions for the co-occurrence of O_3 and $PM_{2.5}$ pollution are investigated. The conclusions are presented in Section 4.

2. Methods

2.1 Observed O_3 and $PM_{2.5}$ concentrations

Hourly concentrations of $PM_{2.5}$ and O_3 in China over the years of 2013-2020 were taken from the public website of CNEMC (https://air.cnemc.cn:18007/, CNEMC, 2022). To ensure data quality, the daily mean $PM_{2.5}$ concentration was calculated when there were valid data for more than 20 h during that day and the MDA8 O_3 concentration was calculated when there were valid data for at least 6 h for each 8 h. For the calculation of monthly and annual mean concentrations, the number of days with valid concentrations had to be more than 15 in each month. The spatial distribution of the 79 valid sites within BTH (37-41°N, 114-118°E, the black rectangle) is shown in Fig. 1. For model evaluation, the observed concentrations were averaged over sites within each of the 0.5° latitude × 0.625° longitude MERRA-2 grid cell. There are 18 model grids in BTH. Note that the observed O_3 concentrations from this network have a unit of μg m^{-3}. For the consistency of observed and simulated O_3 concentrations, 1 μg m^{-3} of O_3 is approximately 0.5 ppb under the conditions of 298 K and 1013 hPa. The observed O_3 concentrations reported by the

CNEMC were under standard conditions of 273 K and 1013 hPa before 31 August 2018 and were under standard conditions of 298 K and 1013 hPa afterwards (http://www.mee.gov.cn/ xxgk2018/xxgk/xxgk01/201808/t20180815_629602.html), which were accounted for as O_3 concentrations were converted to ppb.

According to the National Ambient Air Quality Standard of China (GB3095-2012), O_3 ($PM_{2.5}$) concentration exceeds the national air quality standard if the MDA8 O_3 (daily mean $PM_{2.5}$) concentration is higher than 160 μg m^{-3} (75 μg m^{-3}). In this study, we define O_3 polluted days (hereafter called 'O_3PD') for days with MDA8 O_3 concentration > 160 μg m^{-3}, $PM_{2.5}$ polluted days (hereafter called '$PM_{2.5}$PD') with daily mean $PM_{2.5}$ concentration > 75 μg m^{-3}, and the co-pollution days by O_3 and $PM_{2.5}$ (O_3&$PM_{2.5}$PD) with daily MDA8 O_3 concentration > 160 μg m^{-3} as well as the daily mean $PM_{2.5}$ concentration > 75 μg m^{-3}.

2.2 Reanalyzed meteorological fields

Meteorological fields were obtained from the Version 2 of Modern Era Retrospective-analysis for Research and Application (MERRA2), which were generated by the NASA Global Modeling and Assimilation Office (GMAO). The MERRA2 data have a horizontal resolution of 0.5° latitude × 0.625° longitude and 72 vertical layers (Molod et al., 2015). To analyze the meteorological conditions for O_3&$PM_{2.5}$PD, vertical pressure velocity (OMEGA), planetary boundary layer height (PBLH), temperature (T), relative humidity (RH), surface incoming shortwave flux (SWGDN) are used. Note that the temporal resolution for PBLH, T, and SWGDN is 1h, and that for OMEGA and RH is 3h. Daily mean geopotential heights at 850 and 500 hPa from the National Center for Environmental Prediction (NCEP) and National Center for Atmospheric Research (NCAR) global reanalysis with a resolution of 2.5°

latitude by 2.5° longitude are also utilized in this study.

2.3 Observed aerosol optical depth

We obtained the version 3 datasets of observed daily aerosol optical depth (AOD) of level 2 (improved cloud screened and quality-assured) from Aerosol Robotic Network (AERONET, https://aeronet.gsfc.nasa.gov/new_web/index.html) established by NASA and LOA-PHOTONS (Giles et al., 2019). Three sites in the BTH region have observations available over 2013-2020, including Beijing (39.97°N, 116.38°E), Beijing-CAMS (39.93°N, 116.31°E), and Xianghe (39.75°N, 116.96°E). The AOD values at 440 nm and 675 nm at these three sites are analyzed in this study.

2.4 GEOS-Chem model

We simulated O_3 and $PM_{2.5}$ using the nested version of the 3-D global chemical transport model (GEOS-Chem, version 11-01) driven by the MERRA2 meteorological data. The nested domain was set over Asia (60°-150°E,11°S-55°N) with a horizontal resolution of 0.5° latitude × 0.625° longitude, and the chemical boundary conditions were provided by the global GEOS-Chem simulation with 2.5° latitude × 2.5° longitude horizontal resolution.

The GEOS-Chem model includes fully coupled O_3-NO_x-hydrocarbon and aerosol chemistry mechanism (Bey et al., 2001; Pye et al., 2009) to simulate aerosols including SO_4^{2-} (Park et al., 2004), NO_3^- (Pye et al., 2009), NH_4^+, BC and OC (Park et al., 2003), mineral dust (Fairlie et al., 2007), and sea salt (Alexander et al., 2005) as well as the gas-phase pollutants such as NO_x and O_3. Over the Asian domain, the anthropogenic emissions of OC, BC, carbon monoxide (CO), sulfur dioxide (SO_2),

NO_x, ammonia (NH_3), and VOCs were obtained from the Multi-resolution Emission Inventory for China (MEIC), which includes emissions from industry, power, residential and transportation sectors for years of 2014-2017 (Li et al., 2017; Zheng et al., 2018), 2019 and 2020 (Zheng et al., 2021). Emissions in 2018 were obtained by the interpolation of those in 2017 and 2019 for each grid due to the lack of publicly accessible emission inventories for that year. The biogenic emissions in GEOS-Chem are simulated using MEGAN v2.1 (Guenther et al., 2012).

The hourly O_3 and $PM_{2.5}$ concentrations for the years of 2013-2020 were simulated by the GEOS-Chem model which were driven by MERRA-2 meteorological fields. The model was spined up for 6 months before the integration over the studied time period.

2.5 Process analysis

Process analysis (PA) was applied to identify the relative importance of atmospheric processes in O_3&$PM_{2.5}$PD. PA has been widely used in previous studies to examine the key processes contributing to air pollution episodes (Gonçalves et al., 2009; Dang and Liao, 2019; Gong and Liao, 2019) as well as the interannual and decadal variations of air pollutants (Mu and Liao, 2014; Lou et al., 2015). Five major processes that influence O_3 and $PM_{2.5}$ concentrations were diagnosed at every time step, including net chemical production, dry deposition, horizontal advection, vertical advection, and diffusion, for the regional pollution days (days with more than half of the sites in BTH experiencing pollutions). We carried out PA for O_3SPD (exclude O_3&$PM_{2.5}$PD from O_3PD), $PM_{2.5}$SPD (exclude O_3&$PM_{2.5}$PD from $PM_{2.5}$PD), and O_3&$PM_{2.5}$PD over BTH.

3. Results

3.1 Observed polluted days by O_3 and $PM_{2.5}$

Figure 1a shows the spatial distributions of observed numbers of O_3PD, $PM_{2.5}$PD, and O_3&$PM_{2.5}$PD summed over the warm seasons (April-October) of 2013-2020. The spatial distributions of polluted days in each year are shown in Fig. S1. The numbers of O_3PD, $PM_{2.5}$PD, and O_3&$PM_{2.5}$PD were high in BTH, which were, respectively, 524.3 344.6, and 128.1 days from observations, as the values were averaged over all sites in BTH. The high numbers of O_3PD, $PM_{2.5}$PD, and O_3&$PM_{2.5}$PD in BTH were associated with the highest anthropogenic emissions (NO_x and NMVOCs) in this region (Dang et al., 2021).

Figure 1b shows the numbers of days averaged over all sites in BTH for non-polluted days (NPD, MDA8 O_3 < 80 ppb and $PM_{2.5}$ < 75 μg m^{-3}), O_3PD, O_3&$PM_{2.5}$PD, and $PM_{2.5}$PD in each month of warm seasons from 2013 to 2020. O_3PD and O_3&$PM_{2.5}$PD mainly occurred in May, June, and July, while $PM_{2.5}$PD mainly appeared in April and October. The monthly numbers of O_3&$PM_{2.5}$PD ($PM_{2.5}$PD) declined from 2013 to 2020, with the fastest drop in June, from 7.5 (17.1) days in June 2013 to 1.8 (1.8) days in June 2020. On the contrary, the numbers of O_3PD kept increasing, especially in June, from 10.9 days in June 2013 to 23.6 days in June 2020. The reductions in O_3&$PM_{2.5}$PD were associated with the large reductions in $PM_{2.5}$ since the implementation of the Clean Air Action in 2013.

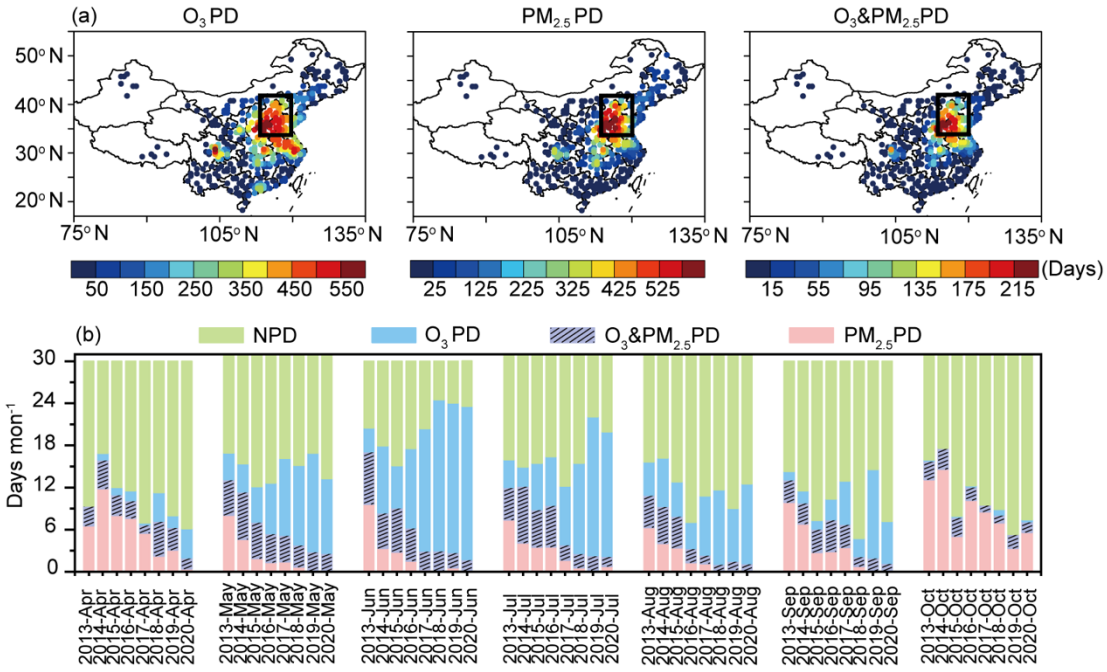

Figure 1. (a) Spatial distributions of observed numbers of O_3PD, $PM_{2.5}$PD, and O_3&$PM_{2.5}$PD summed over April-October of 2013-2020. The solid black rectangle indicates the BTH region. (b) The observed numbers of NPD (non-polluted days, green), O_3PD (blue + purple with slashes), O_3&$PM_{2.5}$PD (purple with slashes), and $PM_{2.5}$PD (pink + purple with slashes) averaged over all sites in BTH from April to October in 2013 to 2020.

Figure 2a shows the linear trends of observed O_3PD, $PM_{2.5}$PD, and O_3&$PM_{2.5}$PD in warm seasons of 2013-2020 averaged over the BTH. O_3PD showed an upward trend of 7.9 days yr^{-1} from 2013 to 2020. However, the numbers of $PM_{2.5}$PD and O_3&$PM_{2.5}$PD decreased over 2013-2020, with linear trends of -11.2 and -3.4 days yr^{-1}, respectively. Figure 2b shows the changes in percentage of O_3&$PM_{2.5}$PD in $PM_{2.5}$PD from 2013 to 2020 for each month. It should be noted that, when $PM_{2.5}$PD occurred, the proportions of O_3&$PM_{2.5}$PD had an upward trend from 2013 to 2020. In May, June, August, and September of 2020, the proportions of O_3&$PM_{2.5}$PD in $PM_{2.5}$PD reached 100%, indicating that $PM_{2.5}$ pollution was accompanied by O_3 pollution in

recent years.

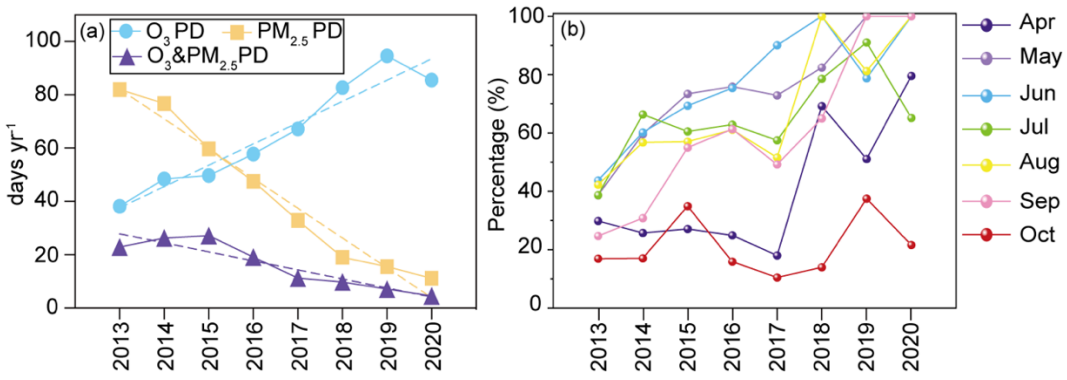

Figure 2. (a) The trends of observed O_3PD, $PM_{2.5}$PD, and O_3&$PM_{2.5}$PD in warm seasons from 2013 to 2020 averaged over all sites in BTH. The blue, yellow and purple solid lines (dashed lines) represent the numbers (liner trend) of O_3PD, $PM_{2.5}$PD, and O_3&$PM_{2.5}$PD, respectively. (b) The percentage of O_3&$PM_{2.5}$PD in $PM_{2.5}$PD for April to October in 2013 to 2020. The polluted days were averaged over all sites in BTH.

3.2 Simulated polluted days and model evaluation

3.2.1 Simulated surface-layer MDA8 O_3 and $PM_{2.5}$ concentrations

Figures 3a and 3b show, respectively, the spatial distributions of simulated and observed surface-layer concentrations of MDA8 O_3 and $PM_{2.5}$ in China, as the concentrations are averaged over the warm seasons (April-October) of 2013-2020. The concentrations of MDA8 O_3 and $PM_{2.5}$ were both high in BTH. Averaged over BTH and the studied time period, the observed concentrations of MDA8 O_3 and $PM_{2.5}$ were 58.1 ppb and 60.3 μg m^{-3}, respectively, while the simulated values were 68.0 ppb and 61.1 μg m^{-3}, respectively. Figures 3c and 3d compare the time series of observed and simulated daily MDA8 O_3 and $PM_{2.5}$ concentrations averaged over the BTH. The simulated daily concentrations of MDA8 O_3 ($PM_{2.5}$) in eight warm seasons have a normalized mean bias (NMB) of 7.9% (10.6%). The model generally captures the daily variations (peaks and troughs) in the observed MDA8 O_3 and $PM_{2.5}$

concentrations, with R values of 0.80 and 0.72, respectively. It should be noted that mineral dust and sea-salt aerosols were not considered in this study, because they are not the major aerosol components in China and the concentrations are generally low based on previous measurements (Xuan et al., 2000; Ye et al., 2003; Duan et al., 2006; Zhao et al., 2013). However, excluding dust and sea salt may lead to low biases in simulated $PM_{2.5}$ concentrations.

Due to the lack of the publicly accessible long-term observations of $PM_{2.5}$ components in China, we compared the simulated SO_2 and NO_2 (precursors for SO_4^{2-} and NO_3^-) with observations from CNEMC in Fig. S2. The simulated daily mean concentrations of NO_2 (SO_2) agree well with the observations from CNEMC with R of 0.82 (0.78) and MB of -14.9% (9.3%).

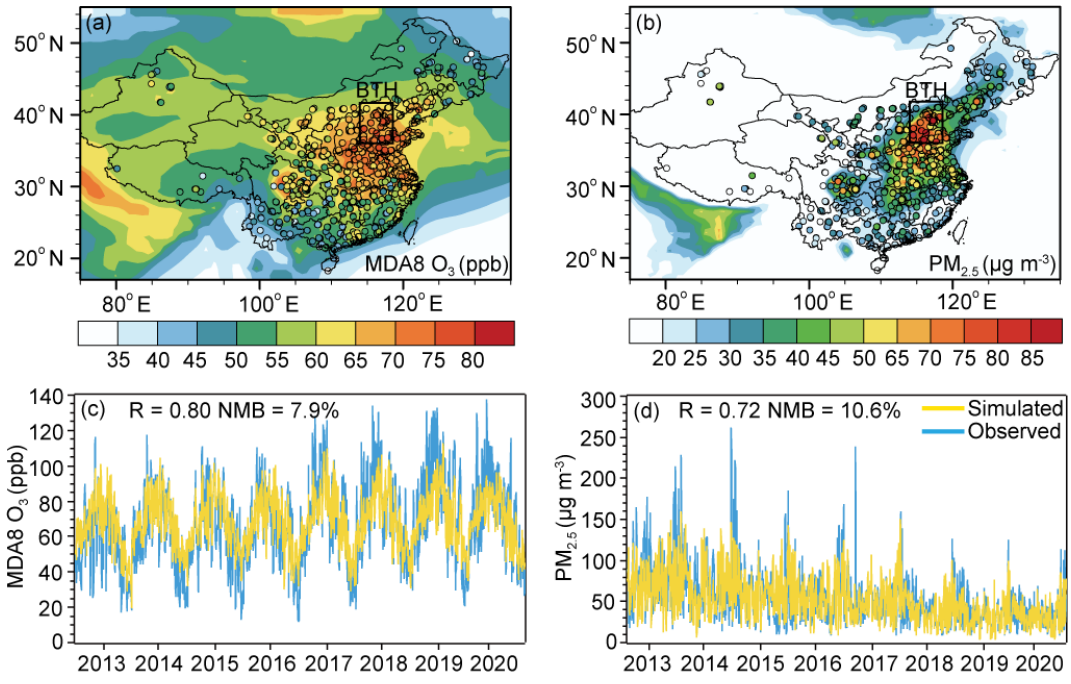

Figure 3. Spatial distributions of simulated (shades) and observed (CNEMC, dots) surface-layer concentrations of (a) MDA8 O_3 (ppb) and (b) $PM_{2.5}$ (μg m^{-3}) averaged over the eight warm seasons (April to October, 2013–2020). The solid black rectangle in (a) and (b) indicates the BTH region. Simulated and observed daily concentrations

of surface-layer (c) MDA8 O_3 and (d) $PM_{2.5}$ averaged over BTH. The correlation coefficient (R) and normalized mean bias (NMB) are also shown for (c) and (d). NMB = $(\sum_{i=1}^{N}(M_i - O_i)/\sum_{i=1}^{N}(O_i)) \times 100\%$, where O_i and M_i are the observed and simulated concentrations, respectively, i refers to the i^{th} day, and N is the total number of days.

3.2.2 Simulated O_3PD, $PM_{2.5}$PD, and O_3&$PM_{2.5}$PD

Figure S3 shows the capability of the model in capturing the polluted days. Although the GEOS-Chem model well reproduces the spatial distributions of observed MDA8 O_3 and $PM_{2.5}$ concentrations, it underestimates the numbers of O_3PD, $PM_{2.5}$PD, and O_3&$PM_{2.5}$PD because of the model's deficiency in capturing the peak concentrations of air pollutants. Such deficiency was also reported in previous studies that used the GEOS-Chem model or the weather Research and Forecasting with Chemistry (WFR-chem) model (Zhang et al., 2016; Ni et al., 2018; Gong and Liao, 2019; Dang and Liao, 2019). Therefore, to identify O_3PD, $PM_{2.5}$PD, and O_3&$PM_{2.5}$PD using model results, we utilized lower thresholds by considering the NMBs of simulated MDA8 O_3 and $PM_{2.5}$ concentrations in each of 18 grids of BTH. Taking the grid of Beijing as an example, simulated MDA8 O_3 and $PM_{2.5}$ had NMBs of -22.0% and -26.9%, respectively, as the simulated concentrations were compared with observations for days with observed concentrations higher than the national air quality standards over the warm seasons of 2013-2020. We then adjusted the threshold of O_3PD in this grid to be 62.4 ppb (80 ppb×78%) and that of $PM_{2.5}$PD to be 54.8 μg m^{-3} (75 μg m^{-3}×73.1%). These adjusted thresholds were also used to identify O_3&$PM_{2.5}$PD. Such approach was also used in previous studies to better capture the pollution events based on the simulations (Dang and Liao, 2019; Gong and Liao, 2019). With the adjusted thresholds, 56-93% of the observed O_3PD, $PM_{2.5}$PD, and O_3&$PM_{2.5}$PD can be captured by the

model (Fig. S3e).

3.2.3 Simulated O_3SPD, $PM_{2.5}$SPD, and O_3&$PM_{2.5}$PD

Since O_3PD or $PM_{2.5}$PD encompasses O_3&$PM_{2.5}$PD, we further define O_3 single pollution days (hereafter called "O_3SPD", which is to exclude O_3&$PM_{2.5}$PD from O_3PD) and $PM_{2.5}$ single pollution days (hereafter called "$PM_{2.5}$SPD", which is to exclude O_3&$PM_{2.5}$PD from $PM_{2.5}$PD) for the purpose of obtaining the characteristics of different polluted days. Figures 4a and 4b show, respectively, the spatial distributions of numbers of O_3SPD, $PM_{2.5}$SPD, and O_3&$PM_{2.5}$PD from observations and from the GEOS-Chem model using the adjusted thresholds. Considering the total of polluted days in 18 grids in BTH, observed O_3SPD, $PM_{2.5}$SPD, and O_3&$PM_{2.5}$PD were, respectively, 3937, 3698, and 2024 days, in which 75.0% (2954/3937), 58.1% (2148/3698), and 79.7% (1614/2024) were captured by observation and simulation simultaneously (Fig. 4c). In addition, the numbers of observed and captured O_3SPD, $PM_{2.5}$SPD, and O_3&$PM_{2.5}$PD in each month are shown in Fig. S4. The model has a fairly good capability of capturing the observed polluted days in each month.

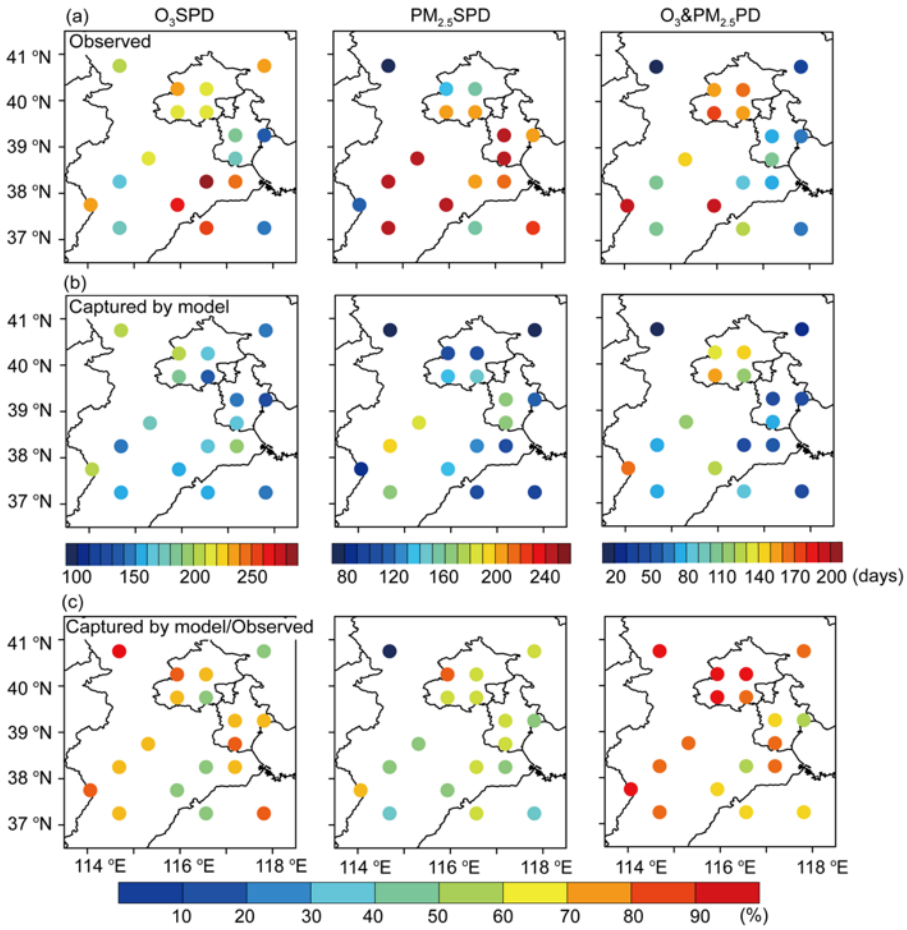

Figure 4. Spatial distributions of (a) observed numbers of O_3SPD, $PM_{2.5}$SPD, and O_3&$PM_{2.5}$PD, (b) numbers of polluted days that were observed and also captured by the GEOS-Chem model with adjusted thresholds, and (c) percentages of observed polluted days that were captured by the model with adjusted thresholds. The values were calculated for the warm months (April to October) of 2013-2020.

3.3 Chemical characteristics of polluted days by O_3 and $PM_{2.5}$

In this section, to investigate the chemical characteristics of O_3SPD, $PM_{2.5}$SPD and O_3&$PM_{2.5}$PD, we present first the simulated atmospheric oxidants in 3.3.1, and then show the simulated surface concentrations and vertical profiles of $PM_{2.5}$ and MDA8 O_3 in 3.3.2 and 3.3.3, respectively, followed by the process analysis in 3.3.4. The observed AOD values to verify the model results are presented in 3.3.5.

3.3.1 Atmospheric oxidants of O_3SPD, $PM_{2.5}$SPD, and O_3&$PM_{2.5}$PD

Figure 5 shows the boxplots of daily concentrations of hydroxyl radical (OH) and total oxidant (O_x = O_3 + NO_2) from the model for days of O_3SPD, $PM_{2.5}$SPD, and O_3&$PM_{2.5}$PD that were observed and also captured by the model (samples in Fig. 4b) in the warm seasons of 2013-2020 in 18 grids of BTH. The levels of OH and O_x characterize the atmospheric oxidation capacity, following Hu et al. (2020) and Chan et al. (2017). The concentrations of OH were the highest in O_3SPD, with an averaged value of 2.8×10^6 molec cm^{-3}, followed by that in O_3&$PM_{2.5}$PD (2.0×10^6 molec cm^{-3}) and in $PM_{2.5}$SPD (1.0×10^6 molec cm^{-3}). Due to the lack of publicly accessible observations of OH in BTH, we compare the simulated OH concentrations with observations reported in the literature (Table S1). The simulated OH concentrations agree closely with the observed values. In Wangdu of BTH, while the observed daily maximum OH concentrations in summer of 2014 were in the range of $5\text{-}15\times10^6$ molec cm^{-3} (Tan et al., 2016), the simulated OH concentrations in the same time period in this work were $3.7\text{-}9.5\times10^6$ molec cm^{-3}. In Beijing in summer of 2017, the observed daily mean OH concentration was 5.8×10^6 molec cm^{-3} (Woodward et al., 2020) and our simulated value was 2.4×10^6 molec cm^{-3}.

The mean values of O_x were, respectively, 178.7, 118.1, and 184.1 μg m^{-3} in O_3SPD, $PM_{2.5}$SPD, and O_3&$PM_{2.5}$PD, indicating that the atmospheric oxidation capacity was strong in O_3&$PM_{2.5}$PD, which favored the production of secondary components of $PM_{2.5}$. Figure 5 also shows sulfur oxidation ratio (SOR, $n\text{-}SO_4^{2-}$ / ($n\text{-}SO_4^{2-}$ + $n\text{-}SO_2$), where $n\text{-}SO_4^{2-}$ and $n\text{-}SO_2$ are the concentrations of SO_4^{2-} and SO_2, respectively) and nitrogen oxidation ratio (NOR, $n\text{-}NO_3^-$ / ($n\text{-}NO_3^-$ + $n\text{-}NO_2$), where $n\text{-}NO_3^-$ and $n\text{-}NO_2$ are the concentrations of NO_3^- and NO_2, respectively). SOR and NOR are measures of the conversion degrees of sulfur and nitrogen, respectively (Zhu et al.,

2019). In O_3SPD, $PM_{2.5}$SPD, and O_3&$PM_{2.5}$PD, the averaged values of SOR were 50.0%, 36.7%, and 49.7%, and those of NOR were 55.4%, 70.0%, and 70.2%, respectively. The high SOR and NOR in O_3&$PM_{2.5}$PD indicated the strong formation of SO_4^{2-} and NO_3^- that were promoted by high atmospheric oxidation capacity. The monthly variations of OH, O_x, and SOR were similar (Fig. 5), with the highest values in summer, owing to the high temperature that promoted high concentrations of oxidants and SOR. It is interesting that SOR and O_x values were higher in O_3&$PM_{2.5}$PD than in O_3SPD or in $PM_{2.5}$SPD during May-August. Similarly, NOR values were higher in O_3&$PM_{2.5}$PD than in O_3SPD or in $PM_{2.5}$SPD in May and July-September. Overall, the O_3&$PM_{2.5}$PD occurred with high levels of atmospheric oxidants, SOR, and NOR, leading to combined increases in O_3 and $PM_{2.5}$ concentrations.

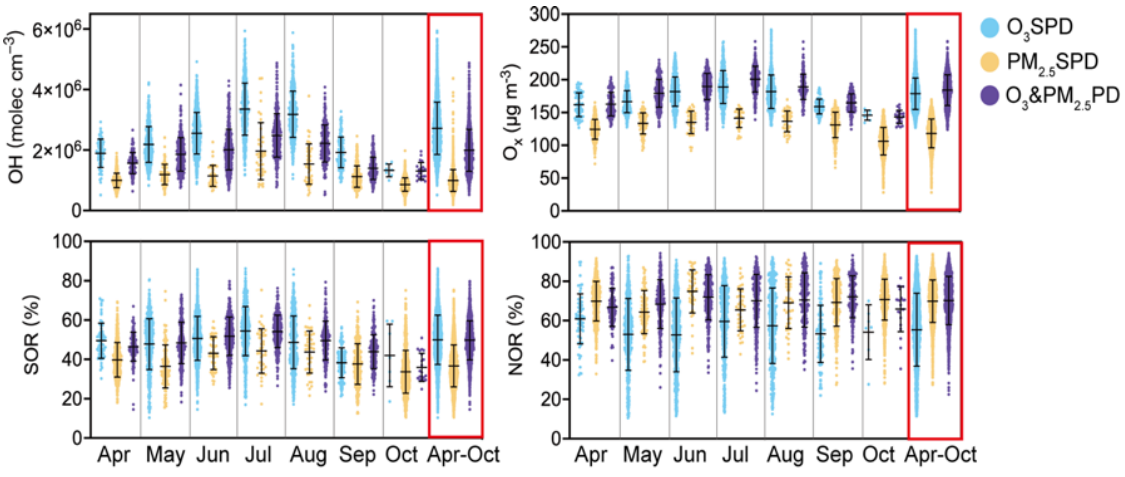

Figure 5. The boxplots of surface-layer hydroxyl radical (OH, molec cm^{-3}), total oxidant (O_x, μg m^{-3}), sulfur oxidation ratio (SOR, %), nitrogen oxidation ratio (NOR, %) for model-captured O_3SPD, $PM_{2.5}$SPD, and O_3&$PM_{2.5}$PD in 18 grids of BTH in the months of April to October from 2013 to 2020. The whiskers represent the standard deviation, the black line represents the mean value of the samples.

3.3.2 Surface-layer concentrations of $PM_{2.5}$ components in O_3SPD, $PM_{2.5}$SPD, and O_3&$PM_{2.5}$PD

The simulated concentrations of $PM_{2.5}$ components (NO_3^-, NH_4^+, SO_4^{2-}, BC, and OC, averaged over 18 grids of BTH are shown in Fig. 6 for days of O_3SPD, $PM_{2.5}$SPD, and O_3&$PM_{2.5}$PD in the warm seasons of 2013-2020 that were observed and also captured by the model. While the mean concentrations of NO_3^-, NH_4^+, BC, and OC, were all the highest in $PM_{2.5}$SPD, SO_4^{2-} concentration was the highest in O_3&$PM_{2.5}$PD. In O_3SPD, $PM_{2.5}$SPD, and O_3&$PM_{2.5}$PD, the mean concentrations of SO_4^{2-} were 6.2, 9.4, and 11.97 μg m^{-3}, respectively, and the percentages of SO_4^{2-} in $PM_{2.5}$ were 14.9%, 9.0%, and 15.0%, respectively. In July and August, the concentrations of SO_4^{2-} and MDA8 O_3 in O_3&$PM_{2.5}$PD were the highest compared with those in O_3SPD and $PM_{2.5}$SPD (Fig. S5).

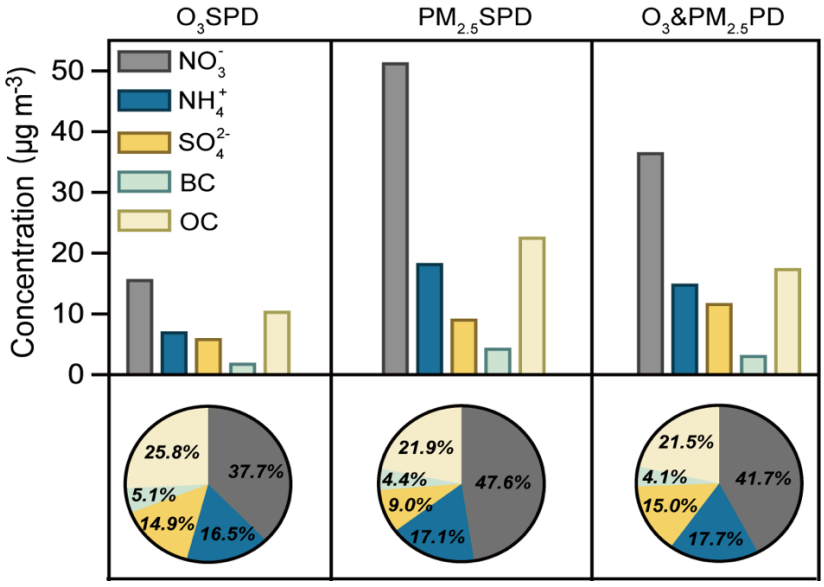

Figure 6. The concentrations of $PM_{2.5}$ components (μg m^{-3}) and percentages of $PM_{2.5}$ components (%) at the surface for NO_3^-, NH_4^+, SO_4^{2-}, BC, and OC. The values were averaged over the model-captured O_3SPD, $PM_{2.5}$SPD, and O_3&$PM_{2.5}$PD in the months of April to October of 2013-2020 in BTH.

Figure 7 presents the hourly concentrations of NO_3^-, NH_4^+, SO_4^{2-}, BC, OC, and O_3 for model-captured O_3SPD, $PM_{2.5}$SPD, and O_3&$PM_{2.5}$PD over all 18 grids of BTH in

the warm seasons from 2013-2020. Concentrations of NO_3^- and NH_4^+ had similarities in diurnal variations, all of which reached the highest values in the early morning (5:00 local time (LT) in O_3SPD and O_3&$PM_{2.5}$PD, 7:00-8:00 LT in $PM_{2.5}$SPD) and had the lowest values in the late afternoon (18:00 LT in O_3SPD and O_3&$PM_{2.5}$PD, 16:00 LT in $PM_{2.5}$SPD). Concentrations of BC and OC peaked at the same time as those of NO_3^- and NH_4^+ and had the lowest values at 15:00 LT in O_3SPD, $PM_{2.5}$SPD, and O_3&$PM_{2.5}$PD. The diurnal variations in NO_3^-, NH_4^+, BC, OC reflected the diurnal variations in PBLH (shown in Fig. S6), which generally reached their highest concentrations before the sudden uplift of PBLH in the early morning (times for uplift of PBLH: 6:00 LT in O_3SPD and O_3&$PM_{2.5}$PD, 7:00 LT in $PM_{2.5}$SPD). Compared to O_3SPD and O_3&$PM_{2.5}$PD, the PBLH of $PM_{2.5}$SPD was lower and uplifted one hour later, which was more favorable for the accumulation of aerosols. During the daytime, PBLH in O_3&$PM_{2.5}$PD was between O_3SPD and $PM_{2.5}$SPD.

It is worth noting that the diurnal variations of SO_4^{2-} were different from those of other aerosol species, with the highest values at 20:00, 9:00, and 16:00 LT in O_3SPD, $PM_{2.5}$SPD, and O_3&$PM_{2.5}$PD, respectively, and the lowest values in early morning and night (5:00 LT in O_3SPD and O_3&$PM_{2.5}$PD, 23:00 LT in $PM_{2.5}$SPD). For the diurnal variation of O_3, the highest values occurred during the daytime (16:00 LT in O_3SPD and O_3&$PM_{2.5}$PD, 15:00 LT in $PM_{2.5}$SPD) and the lowest values appeared at 5:00 LT in all the cases. Therefore, in O_3&$PM_{2.5}$PD, the time of the highest value of SO_4^{2-} was the same as that of O_3, indicating that SO_4^{2-} and O_3 were produced synergistically during the daytime with strong atmospheric oxidation.

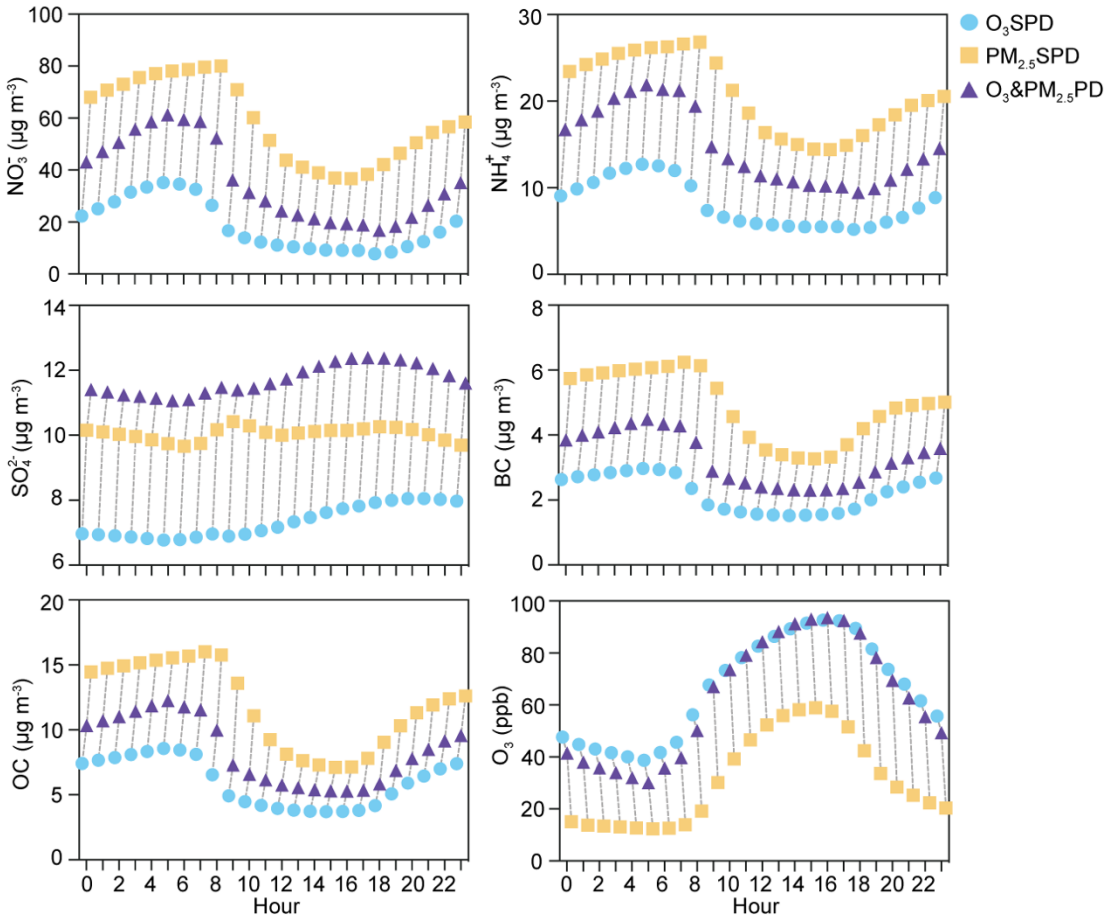

Figure 7. The hourly concentrations of NO_3^-, NH_4^+, SO_4^{2-}, BC, OC, and O_3 averaged over the model-captured O_3SPD, $PM_{2.5}$SPD, and O_3 &$PM_{2.5}$PD in BTH in the months of April to October of 2013-2020.

3.3.3 Vertical distributions of O_3 and $PM_{2.5}$ in O_3SPD, $PM_{2.5}$SPD, and O_3&$PM_{2.5}$PD

The simulated vertical distributions of O_3 and $PM_{2.5}$ averaged over the 18 grids of BTH and the O_3SPD, $PM_{2.5}$SPD, and O_3&$PM_{2.5}$PD in warm seasons of 2013-2020 are shown in Fig. 8. The vertical distribution of O_3 in O_3SPD was similar to that in O_3&$PM_{2.5}$PD (Fig. 8a). In these two cases, concentrations of O_3 increased from the surface to about 975 hPa, remained high between 975 and 819 hPa, and decreased with altitude between 819 and 663 hPa. Although the magnitudes of O_3 were close at the surface (61.9 ppb in O_3&$PM_{2.5}$PD and 58.1 ppb in O_3SPD), the concentration of O_3

averaged over 975 and 819 hPa was 10.4% higher in O_3&$PM_{2.5}$PD than in O_3SPD, which was a very unique feature of O_3&$PM_{2.5}$PD. For the case of $PM_{2.5}$SPD, the concentrations of O_3 were the lowest among the three cases and increased gently with altitude above 975 hPa.

Figure 8b shows the vertical distributions of $PM_{2.5}$ components. In all the cases, $PM_{2.5}$ concentrations were the highest at the surface, and decreased with altitude from the surface to 975 hPa. However, concentrations of $PM_{2.5}$ were quite stable between 975 and 819 hPa for O_3SPD (about 36.4 μg m^{-3}) and O_3&$PM_{2.5}$PD (about 58.1 μg m^{-3}), corresponding to the stable O_3 levels at these altitudes in these two cases (Fig. 8a). For $PM_{2.5}$SPD, while $PM_{2.5}$ concentration at the surface was the highest among the three cases, it decreased rapidly between 975 and 819 hPa. The averaged $PM_{2.5}$ concentration between 975 and 819 hPa was 52.4 μg m^{-3} in $PM_{2.5}$SPD, which was lower than that in O_3&$PM_{2.5}$PD.

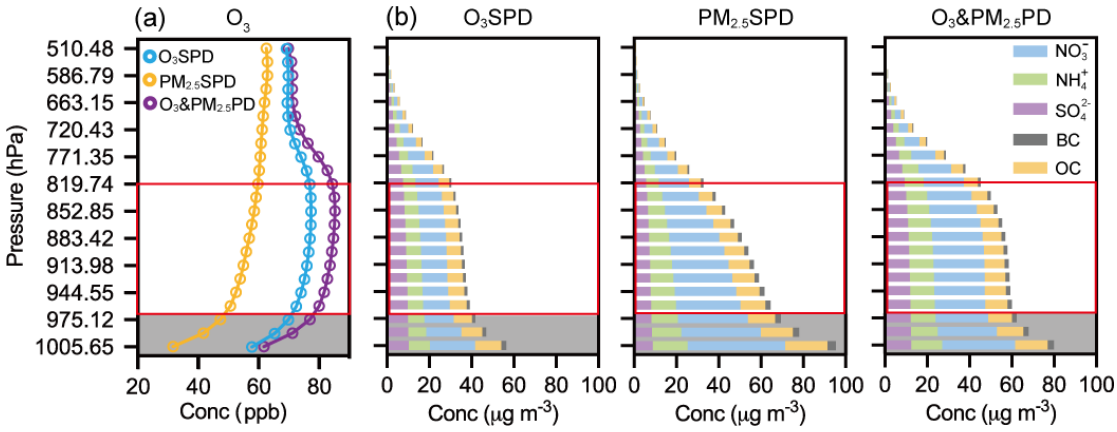

Figure 8. The vertical distributions of (a) concentrations of O_3 (ppb) and (b) $PM_{2.5}$ components (μg m^{-3}) of NO_3^-, NH_4^+, SO_4^{2-}, BC, OC averaged over the model-captured O_3SPD, $PM_{2.5}$SPD, and O_3&$PM_{2.5}$PD in BTH in the months of April to October of 2013-2020.

To further investigate the differences in vertical profiles of NO_3^-, NH_4^+, SO_4^{2-}, BC,

457 OC, and $PM_{2.5}$ in O_3SPD, $PM_{2.5}$SPD, and O_3&$PM_{2.5}$PD, the ratios of concentration at
458 975 hPa to that at the surface as well as the concentration at 819 hPa to that at 975 hPa
459 are shown in Table 1. The concentration of $PM_{2.5}$ decreased largely, with the ratio of
460 $PM_{2.5(975\ hPa)}$ / $PM_{2.5(1005\ hPa)}$ of 0.78 in O_3&$PM_{2.5}$PD and of 0.74 in $PM_{2.5}$SPD. For each
461 of the $PM_{2.5}$ components, the ratios near the surface (from 1005 to 975 hPa, gray shaded
462 area in Fig. 8) were close in the three types of pollution. While the ratios of NO_3^-, NH_4^+,
463 BC, OC were in the range of 0.65-0.80, the ratios of SO_4^{2-} were about 0.93-0.98,
464 indicating that SO_4^{2-} concentrations were quite uniform from the surface to 975 hPa in
465 all three types of pollution.

466 **Table 1.** The ratios at 975 and 1005 hPa (gray shaded area in Fig. 8) and at 819 and
467 975 hPa (red frame in Fig. 8) of NO_3^-, NH_4^+, SO_4^{2-}, BC, OC, and $PM_{2.5}$ in O_3SPD,
468 $PM_{2.5}$SPD, and O_3&$PM_{2.5}$PD in BTH region.

		NO_3^-	NH_4^+	SO_4^{2-}	BC	OC	$PM_{2.5}$
$Conc_{819\ hPa}$/ $Conc_{975\ hPa}$	O_3SPD	0.95	0.90	0.85	0.73	0.73	0.86
	$PM_{2.5}$SPD	0.64	0.68	0.81	0.64	0.63	0.67
	O_3&$PM_{2.5}$PD	0.94	0.91	0.87	0.79	0.77	0.89
$Conc_{975hPa}$/ $Conc_{1005\ hPa}$	O_3SPD	0.65	0.77	0.96	0.69	0.70	0.74
	$PM_{2.5}$SPD	0.72	0.76	0.93	0.67	0.65	0.73
	O_3&$PM_{2.5}$PD	0.72	0.80	0.98	0.76	0.73	0.78

469

470 In the upper layers (975-819 hPa, red rectangle in Fig. 8), the changes in
471 concentrations of pollutants with altitude in $PM_{2.5}$SPD were quite different from those
472 in O_3&$PM_{2.5}$PD and O_3SPD. The decline of $PM_{2.5}$ from 975 to 819 hPa was slow in
473 O_3&$PM_{2.5}$PD ($PM_{2.5(819\ hPa)}$ /$PM_{2.5(975\ hPa)}$ = 0.89) and O_3SPD (0.86) and fast in

$PM_{2.5}$SPD (0.67). Considering that the variation of BC with altitude was mainly driven by meteorology (Sun et al., 2020), the vertical variations of other components that differed significantly from BC indicated the influences of chemical processes. In $PM_{2.5}$SPD, NO_3^-, NH_4^+, OC had about the same ratio as BC (0.64) (with large decreases with height), except for SO_4^{2-} concentration that had a ratio of 0.81. In O_3&$PM_{2.5}$PD, the ratios of NO_3^-, NH_4^+, SO_4^{2-} were, 0.94, 0.91, 0.87, respectively, which were much higher than the value of BC (0.79), indicating NO_3^-, NH_4^+, SO_4^{2-} were quite uniform in the layers of 975-819 hPa with the influence of chemical processes, which will be discussed further in Sect. 3.3.4 below.

3.3.4 Process analyses for O_3SPD, $PM_{2.5}$SPD, and O_3&$PM_{2.5}$PD

The process analysis (PA) is applied to identify the relative importance of atmospheric processes in the three types of pollution. Figure 9 shows the net changes in O_3, NO_3^-, NH_4^+, SO_4^{2-} by the processes of chemical production (Chem), horizontal advection (Horizontal_adv), vertical advection (Vertical_avd), and diffusion (Diff, vertical PBL mixing process) in the GEOS-Chem model, as well as the total of all these processes (i.e., Chem + Diff + Horizontal_avd + Vertical_avd) in O_3SPD, $PM_{2.5}$SPD, and O_3&$PM_{2.5}$PD.

For O_3, the net changes of O_3 by all processes were positive at altitudes of 975-819 hPa in O_3&$PM_{2.5}$PD and O_3SPD, in which Chem had the largest positive contribution (about 1.5 Gg d^{-1}), indicating O_3 is chemically produced at these layers. For NO_3^- and NH_4^+, the nets of all processes increased mass concentrations at 913-819 hPa in O_3&$PM_{2.5}$PD and O_3SPD, in which Chem and Vertical_avd were positive and Chem had the largest positive contribution. The vertical profiles of Chem were similar for NO_3^- and NH_4^+, both of which had the largest positive values at 913-819 hPa (2.83 Gg d^{-1} for NO_3^- and 0.88 Gg d^{-1} for NH_4^+), leading to higher concentrations of NO_3^-

and NH_4^+ in O_3&$PM_{2.5}$PD than in O_3SPD and $PM_{2.5}$SPD. Chem and Diff of SO_4^{2-} were different from those of NO_3^- and NH_4^+. For SO_4^{2-}, Chem was positive from the surface to 510 hPa with a peak around 819 hPa, and Diff was positive at 819-771 hPa but negative from 819 hPa to the surface, which resulted in the uniform SO_4^{2-} profile as shown in Fig. 8. Chem for SO_4^{2-} was the highest around 819 hPa in O_3&$PM_{2.5}$PD, which was related to the strong liquid-phase chemical formation of SO_4^{2-} (Fig. S7). In addition to Chem, Vertical_avd also had positive contributions to the net changes in O_3, NO_3^-, NH_4^+, and SO_4^{2-} at 944-819 hPa. Vertical_avd was negative at 819 hPa and positive between 944 to 819 hPa, implying that the pollutants were transported from 819 hPa to 944 hPa in O_3&$PM_{2.5}$PD.

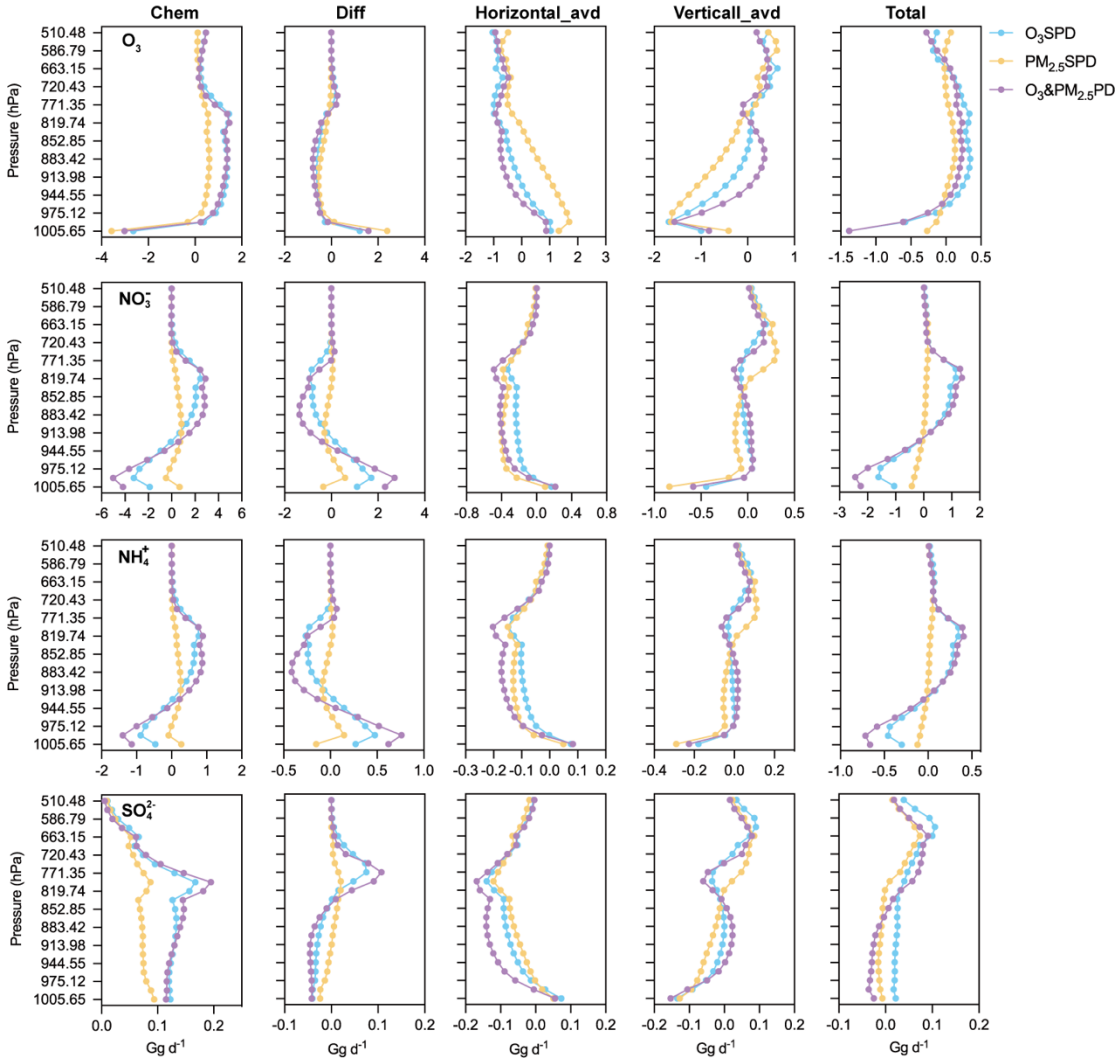

Figure 9. The vertical profiles of net changes in O_3, NO_3^-, NH_4^+, and SO_4^{2-} (Gg d^{-1}) over BTH by each and total of processes. The values were averaged over the model-captured regional O_3SPD, $PM_{2.5}$SPD, and O_3&$PM_{2.5}$PD in April-October of 2013-2020.

Overall, NO_3^-, NH_4^+, and SO_4^{2-} all had larger chemical productions at 913-819 hPa in O_3&$PM_{2.5}$PD compared to those in O_3SPD and $PM_{2.5}$SPD, accompanied by strong vertical transport from 819 hPa to near the surface, resulting in the quite uniform vertical profiles at 975-819 hPa in O_3&$PM_{2.5}$PD. In addition, the vertical profiles of net changes in $PM_{2.5}$ over BTH are shown in Fig. S8 for these three cases. Since NO_3^-, NH_4^+, and SO_4^{2-} were the major components of $PM_{2.5}$, the PA of $PM_{2.5}$ is similar to that of each component.

3.3.5 Observed AOD in O_3SPD, $PM_{2.5}$SPD, and O_3&$PM_{2.5}$PD

To try to support the model result that O_3&$PM_{2.5}$PD had more uniform vertical profile than $PM_{2.5}$SPD from the surface to 819 hPa altitude, we present the scatter plots of observed AOD (at 440 nm and 675 nm) versus observed $PM_{2.5}$ concentrations in O_3SPD, $PM_{2.5}$SPD, and O_3&$PM_{2.5}$PD in Fig. 10. AERONET observations of AOD from 2013 to 2020 are available at three sites in BTH (that is, Beijing (39.97°N, 116.38° E), Beijing-CAMS (39.93°N, 116.31°E), Xianghe (39.75°N, 116.96°E)). At Beijing (39.97°N, 116.38°E), AOD (440nm and 675nm) increased with $PM_{2.5}$ concentration in all three types of pollution. However, under the same levels of surface $PM_{2.5}$ concentration, AOD values in O_3&$PM_{2.5}$PD were higher than in $PM_{2.5}$SPD, implying that the column burdens of aerosols were generally higher in O_3&$PM_{2.5}$PD than in $PM_{2.5}$SPD, which may support the unique vertical distribution of $PM_{2.5}$ in O_3&$PM_{2.5}$PD shown in Fig. 8b. The scatter plots at Beijing-CAMS and Xianghe sites are similar and

are shown in Fig. S9.

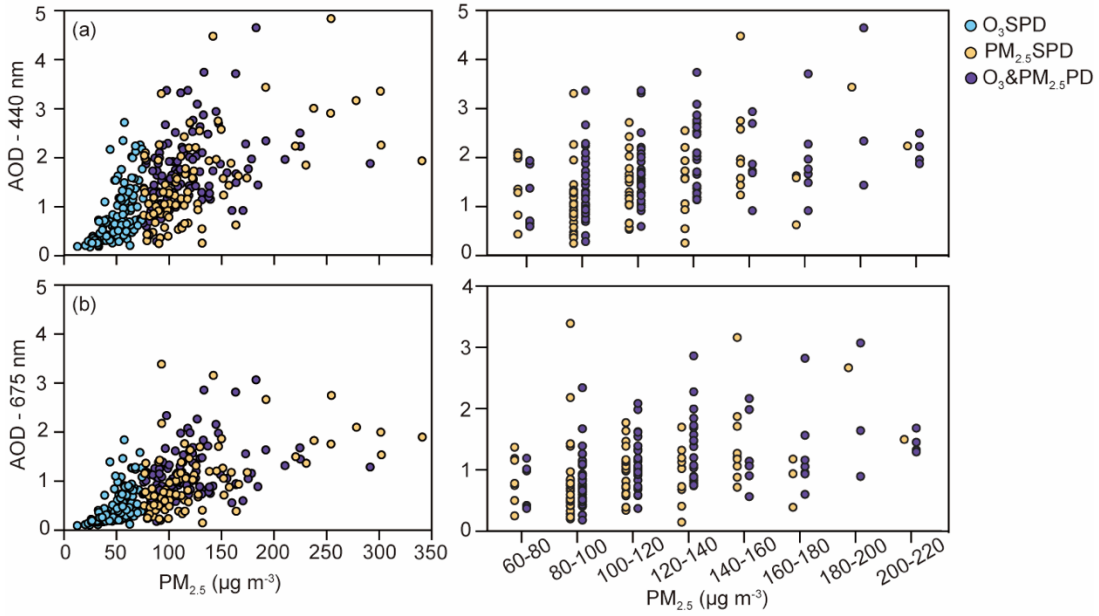

Figure 10. The scatterplots of (a) AOD (440 nm) and (b) AOD (675 nm) versus observed $PM_{2.5}$ concentrations in O_3SPD, $PM_{2.5}$SPD, and O_3&$PM_{2.5}$PD in Beijing (39.97°N, 116.38°E) in April-October of 2013-2020.

3.4 Meteorological conditions for O_3SPD, $PM_{2.5}$SPD, and O_3&$PM_{2.5}$PD over BTH

Figure 11 shows the vertical profiles of RH, T, and OMEGA for O_3SPD, $PM_{2.5}$SPD, and O_3&$PM_{2.5}$PD captured by the model over BTH in the months of April to October form 2013-2020. It should be noted that O_3&$PM_{2.5}$PD had an unique vertical distribution of RH. Near the surface, the values of RH in O_3&$PM_{2.5}$PD were between those in O_3SPD and $PM_{2.5}$SPD. However, in the upper layers (883-771 hPa), O_3&$PM_{2.5}$PD had the highest RH among the three cases with a peak value of 58.2%. As a result, the strongest aqueous chemical production of SO_4^{2-} (aqueous oxidation of SO_2 by H_2O_2) occurred in O_3&$PM_{2.5}$PD around 819 to 771 hPa (Fig. S7**)**. The vertical profiles of temperature were similar in the three types of pollution, with the lowest temperature in $PM_{2.5}$SPD. The vertical profiles of OMEGA were different in the three

cases. In O_3SPD and O_3&$PM_{2.5}$PD, OMEGA had positive values around 819 hPa, indicating a strong sinking airflow, leading to a downward transport of pollutants. Under O_3&$PM_{2.5}$PD, the average values of PBLH and SWGDN were 946.1 m and 257.2 W m^{-2}, respectively, which were higher (lower) than those in $PM_{2.5}$SPD (O_3SPD) (Fig. S10).

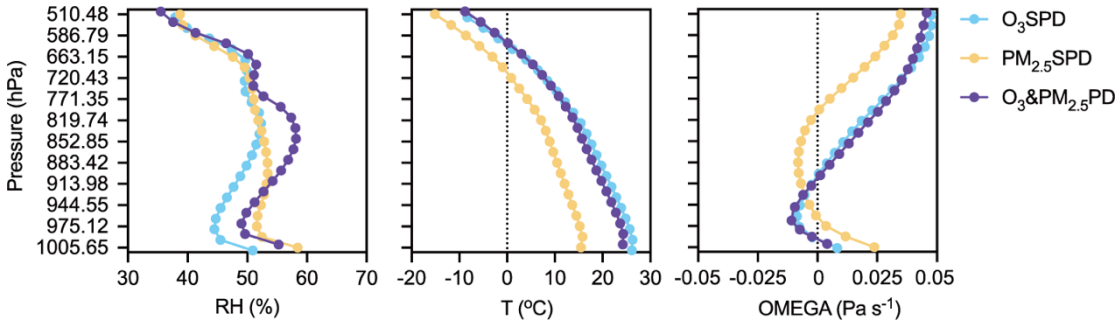

Figure 11. The vertical profiles of RH (%), T (°C), and OMEGA (Pa s^{-1}) averaged over BTH and over the model-captured regional O_3SPD, $PM_{2.5}$SPD, and O_3&$PM_{2.5}$PD in in April-October of 2013-2020.

Figure 12 shows the composited weather patterns for regional O_3SPD, $PM_{2.5}$SPD, and O_3&$PM_{2.5}$PD (over 50% cities in the BTH experienced the pollution) that were captured by the model in April-October of 2013-2020. The weather patterns of O_3&$PM_{2.5}$PD were similar to some extent to those of O_3SPD but were quite different from those of $PM_{2.5}$SPD. In O_3&$PM_{2.5}$PD, the BTH region was controlled by westerlies and an anomalous high-pressure system at 500 hPa (Figure S11). At 850 hPa, BTH was at the west boundary of an anomalous anticyclone, and the associated strong anomalous southerlies at 850 hPa brought moist air to BTH (Fig. S12 and S13), resulting in a high RH that was beneficial to the aqueous chemical production of SO_4^{2-} in O_3&$PM_{2.5}$PD. In O_3SPD, BTH was under the influence of the high pressure ridge of the Western Pacific Subtropical High (WPSH) at 850 hPa. Besides, the Northeast Cold Vortex was located to the southwest of BTH at 850 hPa in O_3SPD, leading to dry and warm conditions, which was favorable for the formation of O_3. In $PM_{2.5}$SPD, the BTH region

was under the influence of both the continental high and the WPSH at 850 hPa. At the surface, BTH was under the influence of a uniform high pressure with very weak winds and hence stagnate atmosphere, which was conducive to the accumulation of $PM_{2.5}$.

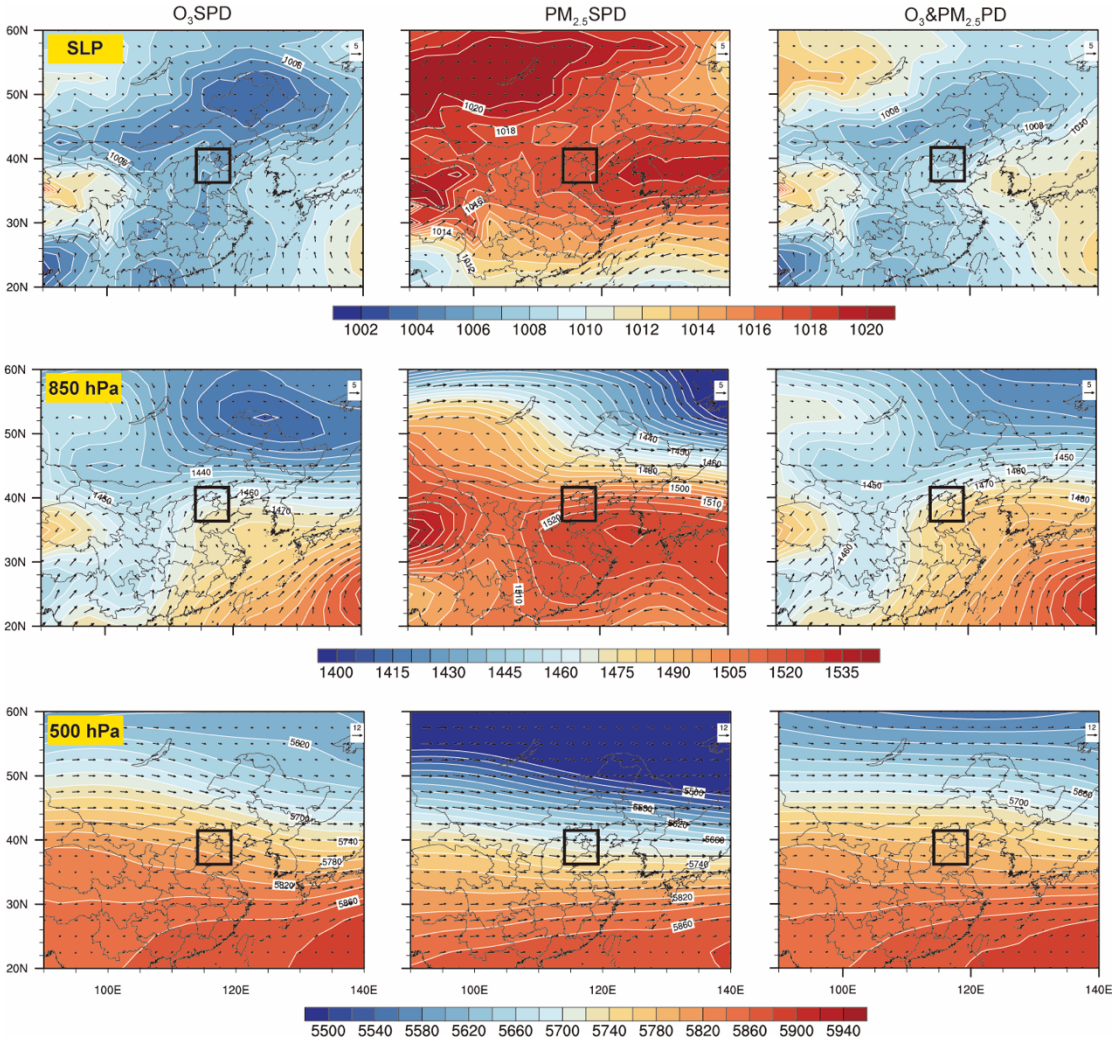

Figure 12. Composites of wind field (m s^{-1}) with SLP (sea level pressure) and with geopotential height at 850 hPa and 500 hPa for regional O_3SPD, $PM_{2.5}$SPD, and O_3&$PM_{2.5}$PD that were captured by the model in April-October of 2013-2020. The solid black rectangle indicates BTH region.

4. Conclusions

We used the observed hourly concentrations of O_3 and $PM_{2.5}$ from CNEMC and the model results from the nested-grid version of the GEOS-Chem model to examine

585 the chemical and physical characteristics of the co-polluted days by O_3 and $PM_{2.5}$
586 (O_3&$PM_{2.5}$PD) over the BTH region for eight warm seasons (April-October) from
587 2013 to 2020. The characteristic of O_3&$PM_{2.5}$PD were compared with those of the
588 polluted days by O_3 alone (O_3SPD) and by $PM_{2.5}$ alone ($PM_{2.5}$SPD). In April-October
589 of 2013-2020, the observed O_3SPD, $PM_{2.5}$SPD, and O_3&$PM_{2.5}$PD were 2954, 2148,
590 and 1614 days, respectively, in which 75.0% (2954/3937), 58.1% (2148/3698), and
591 79.7% (1614/2024) were captured by the GEOS-Chem model, respectively. We
592 carried out composited analyses of the chemical and physical characteristics for
593 O_3SPD, $PM_{2.5}$SPD, and O_3&$PM_{2.5}$PD by using the samples (days) captured by both
594 the observations and the model.

595 The chemical characteristics of O_3&$PM_{2.5}$PD were found to be different from
596 those of O_3SPD, $PM_{2.5}$SPD at the surface. O_3&$PM_{2.5}$PD occurred with high levels of
597 atmospheric oxidants (high OH and O_x), with higher SOR and NOR compared to those
598 in O_3SPD and $PM_{2.5}$SPD, leading to high concentrations of both O_3 and $PM_{2.5}$. At the
599 surface, the composited concentrations of NO_3^-, NH_4^+, BC, and OC were the highest in
600 $PM_{2.5}$SPD, while the composited concentration of SO_4^{2-} was the highest in
601 O_3&$PM_{2.5}$PD. There was a strong formation of SO_4^{2-} during the daytime in
602 O_3&$PM_{2.5}$PD in the oxidative atmosphere.

603 We also found unique features of the vertical distributions of O_3 and $PM_{2.5}$ in
604 O_3&$PM_{2.5}$PD. Concentrations of $PM_{2.5}$ were stable and high between 975 and 819 hPa
605 in O_3&$PM_{2.5}$PD, unlike those in $PM_{2.5}$SPD that decreased rapidly with the altitude. In
606 O_3&$PM_{2.5}$PD, the vertical profiles of NO_3^-, NH_4^+, and SO_4^{2-} were quite uniform at
607 975-819 hPa, corresponding to the stable O_3 concentrations at these altitudes. The
608 process analysis (PA) showed that NO_3^-, NH_4^+, and SO_4^{2-} all had larger chemical
609 productions at altitudes of 913-819 hPa in O_3&$PM_{2.5}$PD compared to those in O_3SPD

and $PM_{2.5}$SPD. The chemical production of SO_4^{2-} had large positive values from the surface to about 500 hPa. The Vertical_avd also had positive contributions to the net changes in O_3, NO_3^-, NH_4^+, and SO_4^{2-} at 944-819 hPa in O_3&$PM_{2.5}$PD. Therefore, the strong chemical productions at 913-819 hPa accompanied by the downward transport resulted in the quite uniform vertical profiles at 975-819 hPa in O_3&$PM_{2.5}$PD.

Figure 13 summarizes the chemical and physical characteristics in O_3&$PM_{2.5}$PD, O_3SPD, and $PM_{2.5}$SPD in the BTH region. In O_3&$PM_{2.5}$PD, the strong chemical productions of O_3, NO_3^-, NH_4^+, and SO_4^{2-} occurred at high altitudes of 913-819 hPa where RH was high, and the accompanied downward airflow caused the stable concentrations at 944-819 hPa. The composited PBLH in O_3&$PM_{2.5}$PD was about 946.1 m, and the strong mixed diffusion underneath the PBLH led to high concentrations of pollutants at the ground level. In contrast, O_3SPD occurred in hot and dry atmosphere with composited PBLH of 1073.5 m. Strong O_3 chemical production occurred around 819 hPa, and O_3 was then transported to the surface by downward air flow. The atmosphere was stable and stagnate when $PM_{2.5}$SPD occurred, with the lowest PBLH of 681.8 m. High RH (high chemical formation of $PM_{2.5}$) and the accumulation of aerosols led to the highest surface-layer $PM_{2.5}$ in $PM_{2.5}$SPD.

To summarize, O_3&$PM_{2.5}$PD were characterized by high O_x, SOR, and NOR, uniform vertical profiles at 975-819 hPa, which were caused by an anomalous high-pressure system at 500 hPa, strong southerlies and high RH at 850 hPa. Meteorological parameters around 850 hPa promoted strong chemical production of secondary aerosols and downward transport, resulting in the unique vertical profiles and high surface concentrations in O_3&$PM_{2.5}$PD.

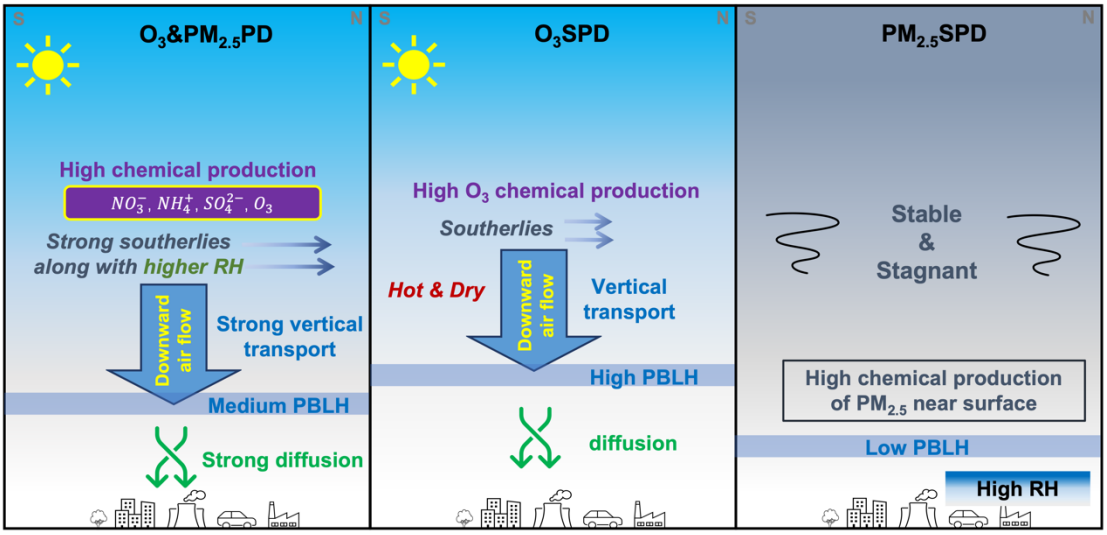

633

634 **Figure 13.** A schematic diagram of chemical and physical and characteristics in

635 O_3SPD, $PM_{2.5}$SPD, and O_3&$PM_{2.5}$PD in BTH region.

Data availability.

The GEOS-Chem model is available at https://geos-chem.seas.harvard.edu (last access: 5 August 2022). The observed hourly surface concentrations of air pollutants are derived from the China National Environ- mental Monitoring Center (https://air.cnemc.cn:18007/, CNEMC, 2022). The simulation results are available upon request from the corresponding author (hongliao@nuist.edu.cn).

Author contributions.

HD and HL conceived the study and designed the experiments. HD performed model simulations and analysed the data. KL, XY, YY, JZ, JJ, and BL provided useful comments on the paper. HD and HL prepared the paper, with contributions from all co-authors.

Competing interests.

The authors declare that they have no conflict of interest.

Acknowledgements.

We acknowledge the CNEMC for making their data publicly available. We acknowledge the efforts of GEOS-Chem working groups for developing and managing the model.

Financial support.

This work was supported by the National Natural Science Foundation of China (Grant No. 42021004), the National Key Research and Development Program of China (Grant No. 2019YFA0606800), and the Carbon Peak Carbon Neutral Science and Technology Innovation Foundation of Jiangsu Province (BK20220031).

References

Alexander, B., Park, R. J., Jacob, D. J., Li, Q. B., Yan- tosca, R. M., Savarino, J., Lee, C. C. W., and Thiemens, M. H.: Sulfate formation in sea-salt aerosols: Constraints from oxygen isotopes, J. Geophys. Res.-Atmos., 110, D10307, https://doi.org/10.1029/2004jd005659, 2005.

Bey, I., Jacob, D. J., Yantosca, R. M., Logan, J. A., Field, B. D., Fiore, A. M., Li, Q. B., Liu, H. G. Y., Mickley, L. J., and Schultz, M. G.: Global modeling of tropospheric chemistry with assimilated meteorology: Model description and evaluation, J. Geophys. Res.-Atmos., 106, 23073–23095, https://doi.org/10.1029/2001jd000807, 2001.

Chu, B. W., Ma, Q. X., Liu, J., Ma, J. Z., Zhang, P., Chen, T. A., Feng, Q. C., Wang. C. Y., Yang, N., Ma, H. N., Ma, J. J., Russell, A. G., He, H.: Air Pollutant Correlations in China: Secondary Air Pollutant Responses to NO_x and SO_2 Control, Environ. Sci. Tech. Let., 7(10), 695-700, http://dx.doi.org/10.1021/acs.estlett.0c00403, 2020.

Dai, H. B., Zhu, J., Liao, H., Li, J. D., Liang, M. X., Yang, Y., Yue, X.: Co-occurrence of ozone and $PM_{2.5}$ pollution in the Yangtze River Delta over 2013-2019: spatiotemporal distribution and meteorological conditions, Atmos. Res., 249, 105363, https://doi.org/10.1016/j.atmosres.2020.105363, 2021.

Dang, R. J. and Liao, H.: Severe winter haze days in the Beijing-Tianjin-Hebei region from 1985-2017 and the roles of anthropogenic emissions and meteorology, Atmos. Chem. Phys., 19, 10801-10816, https://doi.org/10.5194/acp-19-10801-2019, 2019.

685 Dang, R. J., Liao, H., and Fu, Y.: Quantifying the anthropogenic and meteorological
686 influences on summertime surface ozone in China over 2012-2017, Sci. Total.
687 Environ., 754, 142394, https://doi:10.1016/j.scitotenv.2020.142394, 2021.
688 Duan, F., He, K., Ma, Y., Yang, F., Yu, X., Cadle, S. H., Chan, T., and Mulawa, P. A.:
689 Concentration and chemical characteristics of PM2.5 in Beijing, China: 2001–
690 2002, Sci. Total Environ., 355(1–3), 264–275,
691 https://doi:10.1016/j.scitotenv.2005.03.001, 2006.
692 Fairlie, T. D., Jacob, D. J., and Park, R. J.: The impact of transpacific transport of
693 mineral dust in the United States, Atmos. Environ., 41, 1251–1266,
694 https://doi.org/10.1016/j.atmosenv.2006.09.048, 2007.
695 Gao, Y. and Ji, H. B.: Microscopic morphology and seasonal variation of health effect
696 arising from heavy metals in $PM_{2.5}$ and PM_{10}: One-year measurement in a densely
697 populated area of urban Beijing, Atmos. Res., 212, 213–226, https://doi.org/
698 10.1016/j.atmosres.2018.04.027, 2018.
699 Giles, D. M., Sinyuk, A., Sorokin, M. S., Schafer, J. S., Lyapustin, A.: Advancements
700 in the aerosol robotic network (aeronet) version 3 database – automated near real-
701 time quality control algorithm with improved cloud screening for sun photometer
702 aerosol optical depth (aod) measurements, Atmos. Meas. Tech., 12, 169–209,
703 https://doi.org/10.5194/amt-12-169-2019. 2019.
704 Gonçalves, M., Jiménez-Guerrero, P., and Baldasano, J. M.: Contribution of
705 atmospheric processes affecting the dynamics of air pollution in South-Western
706 Europe during a typical summer-time photochemical episode, Atmos. Chem. Phys.,

9, 849–864, https://doi.org/10.5194/acp-9-849-2009, 2009.

Gong, C. and Liao, H.: A typical weather pattern for the ozone pollution events in North China, Atmos. Chem. Phys., 19, 13725-13740, https://doi.org/10.5194/acp-19-13725-2019, 2019.

Gong, C., Liao, H., Zhang, L., Yue, X., Dang, R. J., Yang, Y.: Persistent ozone pollution episodes in North China exacerbated by regional transport, Environ. Pollut., 265, 115056, https://doi:10.1016/j.envpol.2020.115056, 2020.

Guenther, A. B., Jiang, X., Heald, C. L., Sakulyanontvittaya, T., Duhl, T., Emmons, L. K., and Wang, X.: The Model of Emissions of Gases and Aerosols from Nature version 2.1 (MEGAN2.1): an extended and updated framework for mod- eling biogenic emissions, Geosci. Model Dev., 5, 1471–1492, https://doi.org/10.5194/gmd-5-1471-2012, 2012.

Jiang, N., Li, L., Wang, S., Li, Q., Dong, Z., Duan, S., Zhang, R., Li, S.: Variation tendency of pollution characterization, sources, and health risks of $PM_{2.5}$-bound polycyclic aromatic hydrocarbons in an emerging megacity in China: based on three-year data, Atmos. Res., 217, 81–92, https://doi.org/10.1016/j.atmosres.2018.10.023, 2019.

Li, K., Jacob, D. J., Liao, H., Zhu, J., Shah, V., Shen, L., Bates, K., Zhang, Q., Zhai, S. X.: A two-pollutant strategy for improving ozone and particulate air quality in China, Nat. Geosci., 12, 906–910, https://doi.org/10.1038/s41561-019-0464-x, 2019.

Li, K., Jacob, D. J., Shen, L., Lu, X., Smedt, D. I., Liao, H.: Increases in surface ozone

729 pollution in China from 2013 to 2019: anthropogenic and meteorological
730 influences, Atmos. Chem. Phys., 20, 11423-11433, https://doi.org/10.5194/acp-
731 20-11423-2020, 2020.
732 Li, M., Wang, L., Liu, J.: Exploring the regional pollution characteristics and
733 meteorological formation mechanism of $PM_{2.5}$ in North China during 2013-2017,
734 Environ. Int., 134, 105283, https://doi.org/10.1016/j.envint.2019.105283, 2019.
735 Li, M., Zhang, Q., Kurokawa, J.-I., Woo, J.-H., He, K., Lu, Z., Ohara, T., Song, Y.,
736 Streets, D. G., Carmichael, G. R., Cheng, Y., Hong, C., Huo, H., Jiang, X., Kang,
737 S., Liu, F., Su, H., and Zheng, B.: MIX: a mosaic Asian anthropogenic emission
738 inventory under the international collaboration framework of the MICS-Asia and
739 HTAP, Atmos. Chem. Phys., 17, 935–963, https://doi.org/10.5194/acp-17-935-
740 2017, 2017.
741 Liu, Y. X., Zhao, Q. B., Hao, X., Zhao, J. R., Zhang, Y., Yang, X., Fu, Q. Y., Xu, X. Y.,
742 Wang, X. F., Huo, J. T., Chen, J. M.: Increasing surface ozone and enhanced
743 secondary organic carbon formation at a city junction site: An epitome of the
744 Yangtze River Delta, China (2014–2017), Environ. Pollut., 265, 0269-7491,
745 https://doi.org/10.1016/j.envpol.2020.114847, 2020.
746 Lou, S. J., Liao, H., Yang, Y., and Mu, Q.: Simulation of the interannual variations of
747 tropospheric ozone over China: Roles of variations in meteorological parameters
748 and anthropogenic emissions, Atmos. Environ., 122, 839–851,
749 https://doi.org/10.1016/j.atmosenv.2015.08.081, 2015.
750 Molod, A., Takacs, L., Suarez, M., and Bacmeister, J.: Development of the GEOS-5

751 atmospheric general circulation model: evolution from MERRA to MERRA2,
752 Geosci. Model Dev., 8, 1339–1356, https://doi.org/10.5194/gmd-8-1339-2015,
753 2015.
754 Mu, Q. and Liao, H.: Simulation of the interannual varia- tions of aerosols in China:
755 role of variations in meteo- rological parameters, Atmos. Chem. Phys., 14, 9597–
756 9612, https://doi.org/10.5194/acp-14-9597-2014, 2014.
757 Nan, J. L., Wang, S. S., Guo, Y. L., Xiang, Y. J., Zhou. B.: Study on the daytime OH
758 radical and implication for its relationship with fine particles over megacity of
759 Shanghai, China, Atmos. Environ., 154, 167-178,
760 https://doi.org/10.1016/j.atmosenv.2017.01.046, 2017.
761 Ni, R., Lin, J., Yan, Y., and Lin, W.: Foreign and domestic contributions to springtime
762 ozone over China, Atmos. Chem. Phys., 18, 11447–11469,
763 https://doi.org/10.5194/acp-18-11447- 2018, 2018.
764 Park, R. J., Jacob, D. J., Chin, M., and Martin, R. V.: Sources of carbonaceous aerosols
765 over the United States and implica- tions for natural visibility, J. Geophys. Res.-
766 Atmos., 108, 4355, https://doi.org/10.1029/2002jd003190, 2003.
767 Park, R. J., Jacob, D. J., Field, B. D., Yantosca, R. M., and Chin, M.: Natural and
768 transboundary pollution influences on sulfate-nitrate-ammonium aerosols in the
769 United States: Im- plications for policy, J. Geophys. Res.-Atmos., 109, D15204,
770 https://doi.org/10.1029/2003jd004473, 2004.
771 Pye, H. O. T., Liao, H., Wu, S., Mickley, L. J., Jacob, D. J., Henze, D. K., and Seinfeld,
772 J. H.: Effect of changes in climate and emissions on future sulfate-nitrate-

773 ammonium aerosol lev- els in the United States, J. Geophys. Res.-Atmos., 114,
774 D01205, https://doi.org/10.1029/2008jd010701, 2009.
775 Qin, Y., Li, J. Y., Gong, K. J., Wu, Z., Chen, M. D., Qin, M. M., Huang, L., Hu, J. L.:
776 Double high pollution events in the Yangtze River Delta from 2015 to 2019:
777 Characteristics, trends, and meteorological situations, Sci. Total. Environ., 792,
778 148349, https://doi.org/10.1016/j.scitotenv.2021.148349, 2021.
779 Ren, W., Tian, H., Tao, B., Chappelka, A., Sun, G., Lu, C., Liu, M., Chen, G., Xu, X.:
780 Impacts of tropospheric ozone and climate change on net primary productivity and
781 net carbon exchange of China's forest ecosystems, Glob. Ecol. Biogeogr., 20, 391–
782 406, https://doi.org/10.1111/j.1466-8238.2010.00606.x, 2011.
783 Sun, T., Wu, C. and Wu, D.: Time-resolved black carbon aerosol vertical distribution
784 measurements using a 356-m meteorological tower in Shenzhen, Theor. Appl.
785 Climatol., 140, 1263–1276, https://doi.org/10.1007/s00704-020-03168-6, 2020.
786 Tan, Z. F., Fuchs, H., and Lu, K. D.: Radical chemistry at a rural site (Wangdu) in the
787 North China Plain: Observation and model calculations of OH, HO_2 and RO_2
788 radicals, Atmos. Chem. Phys., 17(1): 663−690, https://doi.org/10.5194/acp-17-
789 663-2017, 2017.
790 Wang, H., Kiang, C., Tang, X., Zhou, X., Chameides, W. L.: Surface ozone: a likely
791 threat to crops in Yangtze delta of China, Atmos. Eviron., 39, 3843–3850,
792 https://doi. org/10.1016/j.atmosenv.2005.02.057, 2005.
793 Wang, X., Manning, W., Feng, Z., Zhu, Y.: Ground-level ozone in China: distribution
794 and effects on crop yields, Environ. Pollut., 147 (2), 394–400, https://

795 doi.org/10.1016/j.envpol.2006.05.006, 2007.
796 Woodward-Massey, R., Slater, E. J., Alen, J.: Implementation of a chemical background
797 method for atmospheric OH measurements by laser-induced fluorescence:
798 characterisation and observations from the UK and China, Atmos. Meas. Tech.,
799 13(6): 3119−3146, https://doi.org/10.5194/amt-13-3119-2020, 2020.
800 Xuan, J., Liu, G., and Du, K.: Dust emission inventory in northern China, Atmos.
801 Environ., 34(26), 4565–4570, https://doi:10.1016/S1352-2310(00) 00203-X, 2000.
802 Ye, B., Ji, X., Yang, H., Yao, X., Chan, C. K., Cadle, S. H., Chan, T., and Mulawa, P.
803 A.: Concentration and chemical composition of PM2.5 in Shanghai for a 1-year
804 period, Atmos. Environ., 37(4), 499–510, https://doi:10.1016/S1352-
805 2310(02)00918-4, 2003.
806 Yue, X., Unger, N., Harper, K., Xia, X., Liao, H., Zhu, T., Xiao, J., Feng, Z., Li, J.:
807 Ozone and haze pollution weakens net primary productivity in China, Atmos.
808 Chem. Phys., 17, 6073–6089, https://doi.org/10.5194/acp-2016-1025, 2017.
809 Zhang, Y. and Wang, Y.: Climate-driven ground-level ozone extreme in the fall over the
810 Southeast United States, P. Natl. Acad. Sci. USA, 113, 10025–10030,
811 https://doi.org/10.1073/pnas.1602563113, 2016.
812 Zhao, X. J., Zhao, P. S., Xu, J., Meng, W., Pu, W. W., Dong, F., He, D., and Shi, Q. F.:
813 Analysis of a winter regional haze event and its formation mechanism in the North
814 China Plain, Atmos. Chem. Phys., 13, 5685–5696, https://doi:10.5194/acp-13-
815 5685-2013, 2013.
816 Zheng, B., Tong, D., Li, M., Liu, F., Hong, C., Geng, G., Li, H., Li, X., Peng, L., Qi, J.,

817 Yan, L., Zhang, Y., Zhao, H., Zheng, Y., He, K., and Zhang, Q.: Trends in China's
818 anthropogenic emissions since 2010 as the consequence of clean air actions,
819 Atmos. Chem. Phys., 18, 14095–14111, https://doi.org/10.5194/acp-18-14095-
820 2018, 2018.
821 Zheng, B., Zhang, Q., Geng, G., Chen, C., Shi, Q., Cui, M., Lei, Y., He, K.: Changes in
822 China's anthropogenic emissions and air quality during the COVID-19 pandemic
823 in 2020, Earth Syst. Sci. Data, 13, 2895–2907, https://doi.org/10.5194/essd-13-
824 2895-2021, 2021.
825 Zhu, J., Chen, L., Liao, H., Dang, R. J.: Correlations between $PM_{2.5}$ and ozone over
826 China and associated underlying reasons, Atmosphere, 10(7), 352,
827 https://doi.org/10.3390/atmos10070352, 2019.
828 Zong, L., Yang, Y., and Gao, M.: Large-scale synoptic drivers of co-occurring
829 summertime ozone and $PM_{2.5}$ pollution in eastern China, Atmos. Chem. Phys., 11,
830 9105-9124, https://doi.org/10.5194/acp-21-9105-2021, 2021.